Supporting Information

Electron Transfer from Encapsulated Fe_3C to the Outermost N-doped Carbon Layer for Superior ORR

Javier Quílez-Bermejo[1,*], Ayoub Daouli[2], Sergio García Dalí[1,3], Yingdan Cui[4,5], Andrea Zitolo[6], Jimena Castro-Gutiérrez[1], Mélanie Emo[7], Maria T. Izquierdo[8], William Mustain[4], Michael Badawi[2,9], Alain Celzard[1,10], Vanessa Fierro[1,*].

[1]Université de Lorraine, Centre National de la Recherche Scientifique (CNRS), Institut Jean Lamour (IJL), F-88000, Épinal, France.

[2]Université de Lorraine, CNRS, Laboratoire de Physique et Chimie Théoriques (LPCT), F-54000 Nancy, France.

[3]Departamento de Ciencia de los Materiales e Ingeniería Metalúrgica, Universidad de Oviedo, 33004, Oviedo, Spain

[4]Department of Chemical Engineering, University of South Carolina, Columba, SC United States of America.

[5]Department of Chemical and Biological Engineering, The Hong Kong University of Science and Technology, Kowloon, Hong Kong, China.

[6]Synchrotron SOLEIL, Départementale 128, 91190 Saint Aubin, France.

[7]Université de Lorraine, Institut Jean Lamour (IJL), 54011 Nancy, France.

[8]Instituto de Carboquímica (ICB-CSIC), Miguel Luesma Castán 4, E-50018, Zaragoza, Spain.

[9]Université de Lorraine, CNRS, Laboratoire Lorrain de Chimie Moléculaire (L2CM), F-57000 Metz, France.

[10]Institut Universitaire de France (IUF), F-75231 Paris, France.

Materials and methods

Synthesis of C_1N_1

Guanine (2.5 g, Sigma-Aldrich) was heat-treated in a high-temperature tubular furnace at 700 ºC with a heating rate of 1 ºC min^{-1} under an N_2 flow of 150 mL min^{-1}. Prior to heat treatment, the furnace was purged for 1 hour with the same N_2 flow rate at room temperature. After heat treatment, C_1N_1 samples were obtained.

Synthesis of NC@Fe_3C materials

NC@Fe_3C materials were prepared by ball milling. C_1N_1 (450 mg) was mixed with $FeCl_3 \cdot 6H_2O$ (750 mg) for 30 min in a planetary mill equipped with an agate (50 mL) bowl and (10) balls (PM 100, Retsch) operating at a rotational speed of 500 rpm. The recovered paste was dried and subjected to heat treatment at 900 °C for 1 hour, with a heating rate of 5 ºC min^{-1}, under an N_2 flow of 150 mL min^{-1}. Temperatures ranging from 500 to 1000 ºC were also used to prepare materials for comparison, following the same synthesis procedure. Prior to pyrolysis, the furnace was purged with an N_2 flow of 150 mL min^{-1} for 1 h. After cooling under the same N_2 flow, the NC@Fe_3C materials obtained were immersed in 1 M HCl in an ultrasonic bath for 30 min to remove any residual unreacted metal. The materials were then washed successively on a paper filter with 1 M HCl and distilled water. Finally, the materials were dried overnight in an oven set at 100 ºC.

Physicochemical characterization

Elemental analysis was used to determine C, N, H and O contents using a Vario EL Cube analyzer (Elementar). The materials (2 mg) were heat treated at 1700 ºC in a helium atmosphere containing oxygen. The combustion gases thus obtained were then separated by a chromatographic column and analyzed by a thermal conductivity detector. O was determined and not obtained by difference. X-ray photoelectron spectra (XPS) were obtained using an

ESCAPlus OMICRON spectrometer equipped with a non-monochromatized Mg·Kα X-ray source. Shirley-type background and quantification were processed using CASA software. Peak deconvolution of Fe 2p, N 1s, C 1s and O 1s were performed by least-square fitting using Gaussian-Lorentzian (20:80) curves. Crystalline phases of NC@Fe_3C-*T* materials were determined using a Bruker D8 Advance A25 polycrystalline powder X-ray diffractometer. Structural order at the nanoscale was studied for all NC@Fe3C-T materials by Raman spectroscopy using a Horiba XploRa Raman apparatus equipped with a 50 X long-range objective. The spectra are acquired between 500 and 3500 cm^{-1} with a circularly polarized laser of wavelength 638 nm, filtered at 10 % maximum energy to prevent sample heating, and using a holographic grating of 1200 lines per mm. The intensity ratio between D and G bands (I_D/I_G) was calculated based on the maximum intensity values between 1200 and 1450 cm^{-1} for the D band and 1450 and 1800 cm^{-1} for the G band.

High-resolution transmission electron microscopy (HRTEM) and scanning transmission electron microscopy (STEM) investigations were performed in a JEOL JEM-ARM 200F Cold FEG, operating at 200 kV and equipped with a spherical aberration (Cs) probe and image correctors (0.12 nm point resolution in TEM mode and 0.078 nm in STEM mode). STEM images were obtained in high-angle annular dark-field (HAADF) mode. The chemical composition was studied by energy dispersive X-ray spectroscopy (EDX), collected on a JEOL spectrometer (SDD) in STEM mode.

X-ray absorption spectroscopy (XAS) measurements were carried out at the Fe K-edges in transmission mode at the SAMBA beamline of the SOLEIL synchrotron (France). The beamline is equipped with a sagittally bent double Si (220) crystal monochromator and two Pd-coated mirrors used to remove X-ray harmonics. The catalysts were pelletized into 10 mm diameter disks using boron nitride as a binder. Data were processed using Athena software [1].

The textural properties of the samples were studied by N_2 adsorption measurements performed at -196 °C on a Belsorp Max II manometric sorption analyzer Prior to the adsorption experiments, all samples were outgassed under secondary vacuum for 24 h at 110 ºC. The pore size distributions were obtained using the 2D non-local density functional theory (2D-NLDFT) with SAIEUS® software (Micromeritics), from which the textural properties were calculated, such as: total surface area, $S_{2D\text{-}NLDFT}$, total pore volume, V_T, mesopore volume, V_{MESO}, and micropore volume (pore diameter less than 2.0 nm), V_{MIC} [2].

Electrochemical characterization

Electrochemical experiments were carried out with a rotating ring-disk electrode (RRDE) in a conventional three-electrode cell using an Autolab PGSTAT302 potentiostat. The rotating electrode is equipped with a 5 mm diameter carbon disk and a platinum ring that acts as a second working electrode. A reversible hydrogen electrode (RHE) immersed in the working electrolyte and a graphite rod were used as reference and counter electrodes, respectively.

The working electrodes were prepared as follows: 0.5 mg of NC@Fe_3C-*T* was suspended ultrasonically in 0.125 mL of an aqueous solution of 0.2 wt.% Nafion ® and 20 wt.% isopropanol [3]. 33 µL of the 4 mg mL^{-1} suspension thus obtained was drop-cast on the carbon disk electrode to a catalyst loading of 685 $\mu g \cdot cm^{-2}$. A commercial Pt/C electrocatalyst was also analyzed for comparison. Prior to ORR testing, the Pt/C electrocatalyst underwent electrochemical cycling from 0.0 to 1.25 V vs RHE to clean effectively the platinum surface of any carbon contaminants. The electrocatalytic activity towards the oxygen reduction reaction (ORR) was studied by linear sweep voltammetry (LSV) in O_2-saturated 0.1 M KOH and 0.5 M H_2SO_4 solutions between 1.0 and 0.0 V vs RHE at 1600 rpm and a scan rate of 5 $mV \cdot s^{-1}$. The platinum ring potential was set at 1.5 V vs RHE to calculate the yield of hydrogen peroxide (H_2O_2) during the ORR measurements. Sample stability was studied by

chronoamperometric tests. For this, the working electrode was held at 0.6 V vs RHE for 10,000 s at 1600 rpm, under continuous oxygen saturation.

AEMFC experiments

To produce the gas diffusion electrodes (GDEs) for the anode and cathode, inks were prepared by combining NC@Fe_3C-900, ETFE ionomer powder[4], and isopropanol. The ink was prepared by manually grinding polytetrafluoroethylene (PTFE) with 200 mg of NC@Fe_3C-900 and 1 mL of ultrapure water for 10 min using a mortar and pestle. Then, 1.5 mL of isopropanol was introduced into the mortar and the mixture homogenized for a further 5 min. The ink was subsequently sprayed onto a Toray TGP-H-60 gas diffusion layer (containing 5 wt.% PTFE) using an air-assisted sprayer (Iwata) to prepare the GDEs. The anode electrodes were prepared using a similar method to that described previously [5], with 60 wt.% PtRu/C catalysts.

The anode electrode, cathode electrode and anion-exchange membrane were hydrated with ultrapure water for 20 min and then soaked three times in 1.0 M KOH solution to exchange the polymer from bromide to hydroxide form. The AEM consisted of 20 μm-thick poly(norbornene)-based tetrablock copolymer membrane with an ion-exchange capacity of 3.88 meq·g^{-1} [6–8]. Membranes and GDEs were assembled immediately after functionalization in a Scribner cell with 5 cm^2 active area featuring single-channel serpentine flow fields. Teflon gaskets 152 μm and 203 μm thick were used at the anode and cathode electrodes, respectively, to maintain a compression of approximately 25%. The Scribner 850e fuel cell test station was used to control the AEMFC. The relative humidity (RH) of both cathode- and anode-reacting gases were adjusted to optimize cell performance at an operating temperature of 60 ºC. The gases used in this study comprised ultra-high purity H_2 and O_2 from Airgas.

Structural Models

To comprehensively compare and assess the influence of Fe_3C on catalytic performance, five distinct model systems were designed and tested. Initially, a 1 nm diameter carbon nanotube, saturated with hydrogens atoms at the edges, was modeled to represent the base carbon layer and referred to as C in the manuscript. To investigate the impact of nitrogen doping, an N-doped carbon layer, called NC, was created by partially substituting C atoms with N atoms. Subsequently, a Fe_3C nanoparticle was modeled and incorporated into both the C and NC systems, resulting in two additional models called C@Fe_3C and NC@Fe_3C, respectively. To explore the effect of C layer thickness on the catalytic performance of Fe_3C, a double C-layer was also constructed. The two C-layers were separated by a distance of 0.37 nm, reflecting the experimental results and the model material was denoted as 2NC@Fe_3C in the manuscript. Each system was meticulously designed to isolate and evaluate the specific factors contributing to the overall catalytic behavior studied.

DFT computational details

TGCC supercomputing facility, a high-performance scientific computing resource at CEA, was used for all calculations. Each calculation involved the use of 128 cores, and the optimization of each configuration took over a month of continuous processing.

The electrocatalytic properties of NC@Fe_3C materials were investigated with periodic density functional theory (DFT) calculations[9,10], using the Vienna ab initio simulation package (VASP)[11,12]. The Perdew-Burke-Ernzerhof (PBE) functional, a widely accepted choice within the Generalized Gradient Approximation (GGA) framework, was employed to describe the exchange–correlation interaction[13]. Structural relaxation of all studied configurations was achieved using the conjugate gradient method, with a plane wave cut-off

energy set at 600 eV. The Kohn-Sham self-consistent energy was iterated until convergence, with a criterion of 10^{-6} eV for forces and 0.2 eV nm^{-1} per atom. Brillouin zone sampling used a Gamma-centered mesh at the gamma point.

In order to accurately model the adsorption of various gas molecules, the Grimme dispersion correction (DFT-D3(BJ)) scheme was incorporated to effectively capture van der Waals forces [14,15]. Spin-polarized calculations were conducted for all scenarios, and a Hubbard-like U parameter (4.0) was introduced to address strong correlation effects at the Fe_3C sites, as determined by Wang et al. [16].

In order to reveal the interaction between ORR intermediates gas molecules and NC@Fe_3C, the adsorption energy was computed at 0 K using the formula:

$$\Delta E_{ads} = E_{(NC@Fe3C+guest)} - (E_{NC@Fe3C} + E_{guest}) \quad \textbf{Eq.1}$$

where $E_{(CN@Fe3C+guest)}$ represents the total energy of the NC@Fe_3C model material with a single gas molecule adsorbed, while $E_{CN@Fe3C}$ and E_{guest} are the total energies of the NC@Fe_3C and the isolated gas molecule, respectively.

To assess the impact of the Fe_3C core on charge transfer to molecules adsorbed on the C-layer, the Bader charge difference (ΔQ) was determined using Bader's approach [17]. This method partitions space based on the topological properties of charge density, defining boundaries as surfaces where the charge density gradient has zero flux. The electronic charge difference (ΔQ) is then calculated by:

$$\Delta Q = Q_{(NC@Fe3C+guest)} - (Q_{NC@Fe3C} + Q_{guest}) \quad \textbf{Eq.2}$$

Similarly, here $Q_{(NC@Fe3C+guest)}$ represents the Bader charge of all interacting atoms, while $Q_{NC@Fe3C}$ and Q_{guest} are the Bader charges of the NC@Fe_3C system and the isolated molecule in the gas phase, respectively. Following the same methodology, the variations in electron density (Δρ) induced by the evolution of the chemical system were calculated and then visualized using VESTA software.

Calculation methods for evaluating ORR activity

Methods for assessing ORR activity were used to elucidate the reaction mechanism of selected materials under specific conditions. At a pressure of 1 bar and a temperature of 298.15 K, it is proposed that the ORR proceeds through four proton-coupled electron transfer (PCET) steps:

$$* + O_2 + (H^+ + e^-) \rightarrow OOH^*, \quad \text{(S1)}$$

$$OOH^* + (H^+ + e^-) \rightarrow O^* + H_2O, \quad \text{(S2)}$$

$$O^* + (H^+ + e^-) \rightarrow OH^*, \quad \text{(S3)}$$

$$OH^* + (H^+ + e^-) \rightarrow * + H_2O, \quad \text{(S4)}$$

Here, the asterisk (*) denotes subsequent intermediate species absorbed on the active sites of the catalysts.

To evaluate the differences in free energy associated with these four PCET steps, the computational hydrogen electrode (CHE) method, developed by Nørskov et al.[18] was used. The free energies of the ORR reactions (i.e., (S1) to (S4)) are given by:

$$\Delta G_{OOH^*} = G(OOH^*) - G(H^+) - \mu(e^-) - G(O_2) - G(NC@Fe_3C) \quad \text{(S5)}$$

$$\Delta G_{O^*} = G(O^*) + G(H_2O) - 2\,G(H^+) - 2\,\mu(e^-) - G(O_2) - G(NC@Fe_3C) \quad \text{(S6)}$$

$$\Delta G_{OH^*} = G(OH^*) - 3\,G(H^+) - 3\,\mu(e^-) - G(O_2) - G(NC@Fe_3C) + G(H_2O) \quad \text{(S7)}$$

The expressions for Gibbs free energy (G) and chemical potential (μ) are given by:

$$G = E_{DFT} + ZPE - TS \quad \text{(S8)}$$

$$G(H^+) - \mu(e^-) = \tfrac{1}{2}\, G(H_2) \quad \text{(S9)}$$

where E_{DFT} is the density functional theory energy, ZPE is the zero-point energy, T is the temperature, and S is the entropy. These equations enable us to calculate the free energy differences for each step of the ORR process, providing valuable insights into the reaction mechanism.

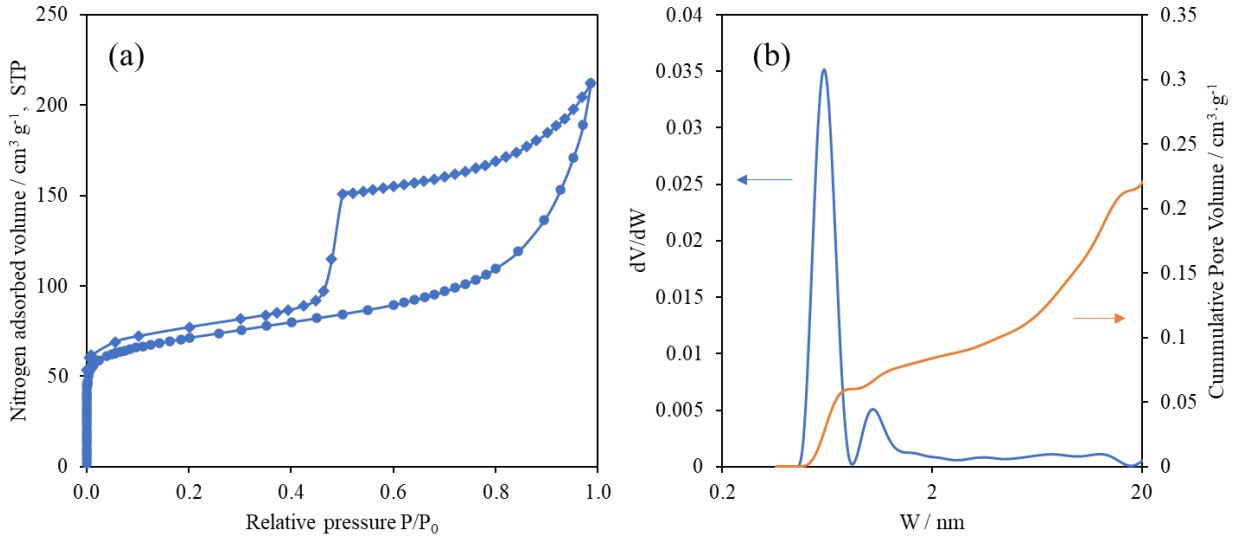

Figure S1: (a) N_2 adsorption-desorption isotherm, and (b) differential and cumulative pore volumes of pristine C_1N_1 material. W represents the pore width and V represents the pore volume.

Table S1: Carbon, oxygen, nitrogen and hydrogen contents obtained from elemental analysis, and Fe content obtained from ICP-OES.

Sample	*C content / wt.%*	*O content / wt.%*	*N content / wt.%*	*H content / wt.%*	*Fe content / wt.%*	*C/N atomic ratio*
C_1N_1	49.0	12.4	36.8	1.7	-	1.3
NC@Fe_3C-500	46.2	20.5	38.3	2.8	2.2	1.2
NC@Fe_3C-700	60.2	10.8	6.5	0.9	9.8	9.3
NC@Fe_3C-800	77.3	9.7	3.3	0.7	8.8	23.4
NC@Fe_3C-900	79.1	9.9	3.1	0.7	14.0	25.5
NC@Fe_3C-1000	83.1	6.0	2.5	0.4	13.3	33.2

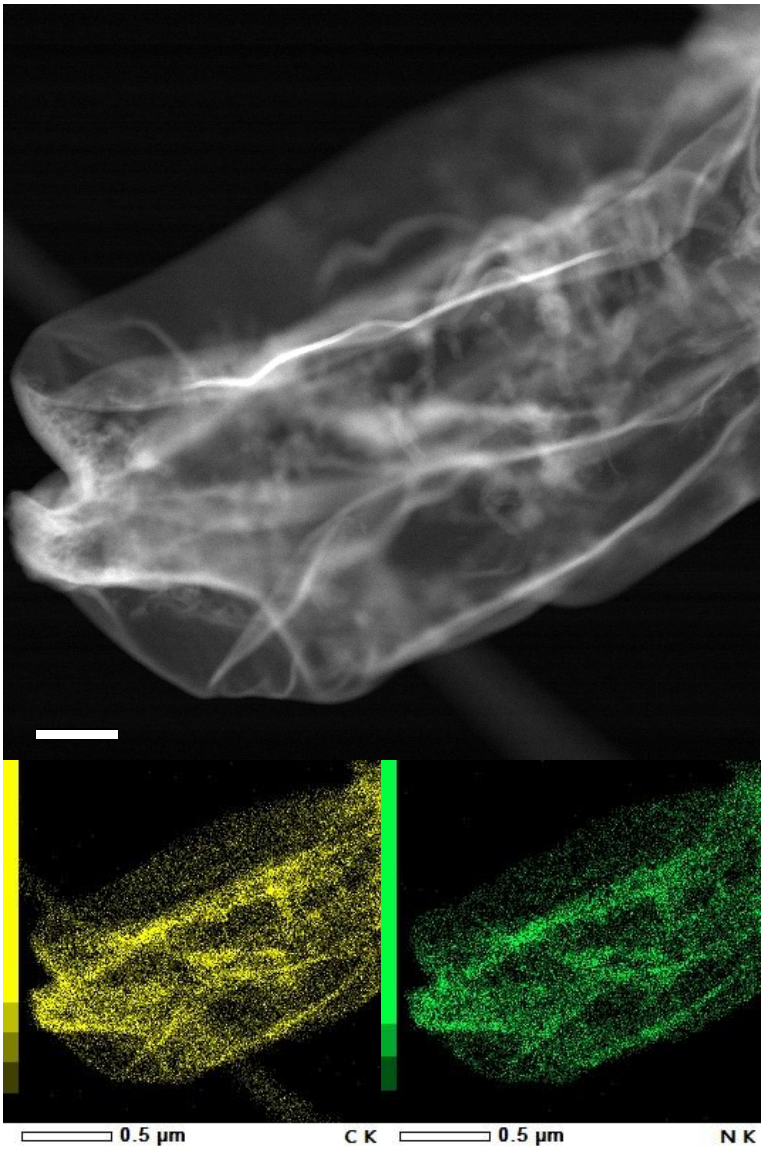

Figure S2: STEM image (in HAADF mode) at low magnification (top) and corresponding EDX mapping of carbon (yellow) and nitrogen (green) of pristine C_1N_1 material.

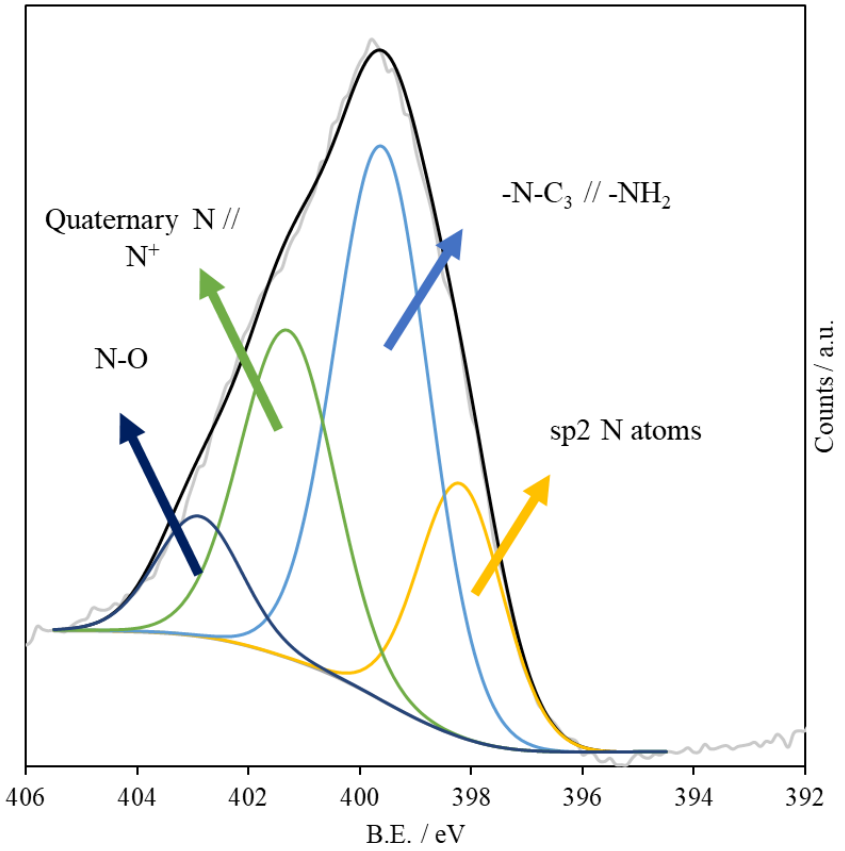

Figure S3: XPS N 1s spectrum of pristine C_1N_1 material. The yellow peak represents sp^2 N atoms, the blue peak represents -N-C_3 or -NH_2-type nitrogen species, the green peak represents quaternary nitrogen or positively charged N atoms, and the dark blue peak represents the oxidized nitrogen species.

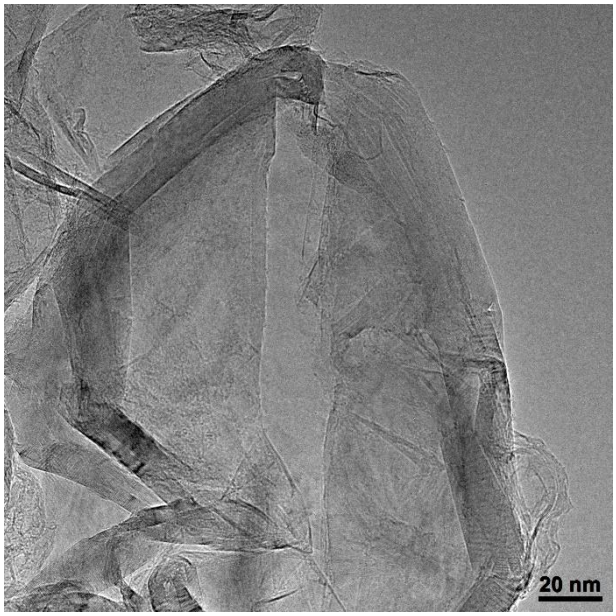

Figure S4: HRTEM image of a graphitic region without metallic nanoparticles in NC@Fe_3C-900.

Table S2: Number of carbon layers, encapsulation thickness and interlayer spacing of NC@Fe_3C-*T* materials.

Sample	*Number of carbon layers*	*Encapsulation thickness / nm*	*Interlayer spacing / nm*	*Fe-based dominant phase*
NC@Fe_3C-500	-	-	-	-
NC@Fe_3C-700	8	3	0.385	$Fe^{3+}O(OH)$ / Fe_3C
NC@Fe_3C-800	21	8	0.378	Fe_3C
NC@Fe_3C-900	32	12	0.370	Fe_3C
NC@Fe_3C-1000	68	25	0.365	Fe_3C

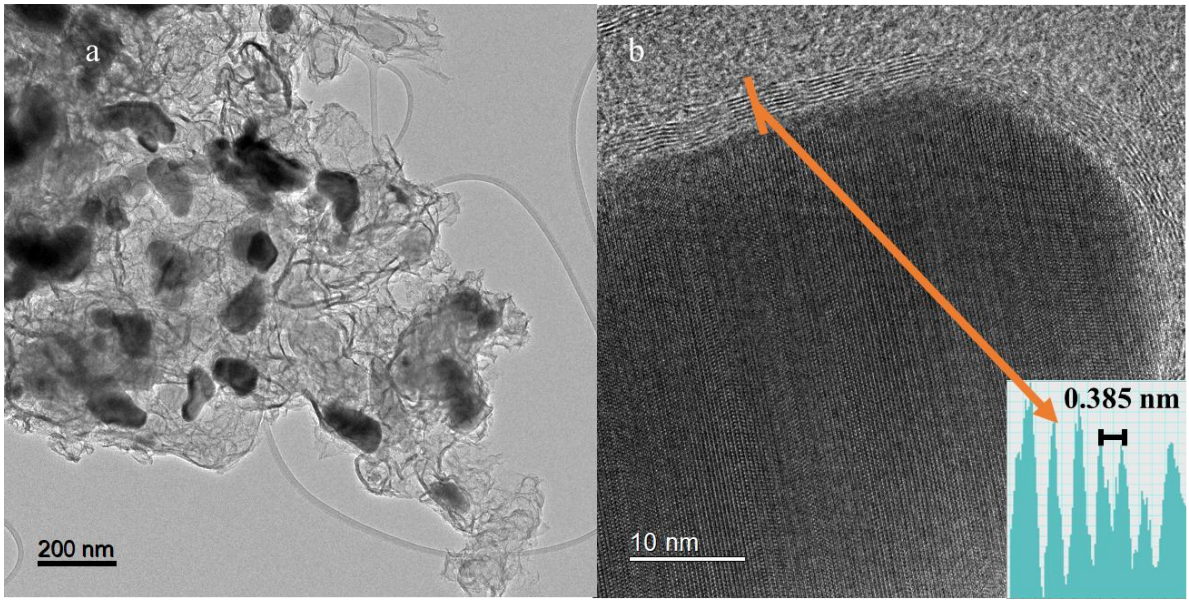

Figure S5: HRTEM images of NC@Fe_3C-700 at two different magnifications.

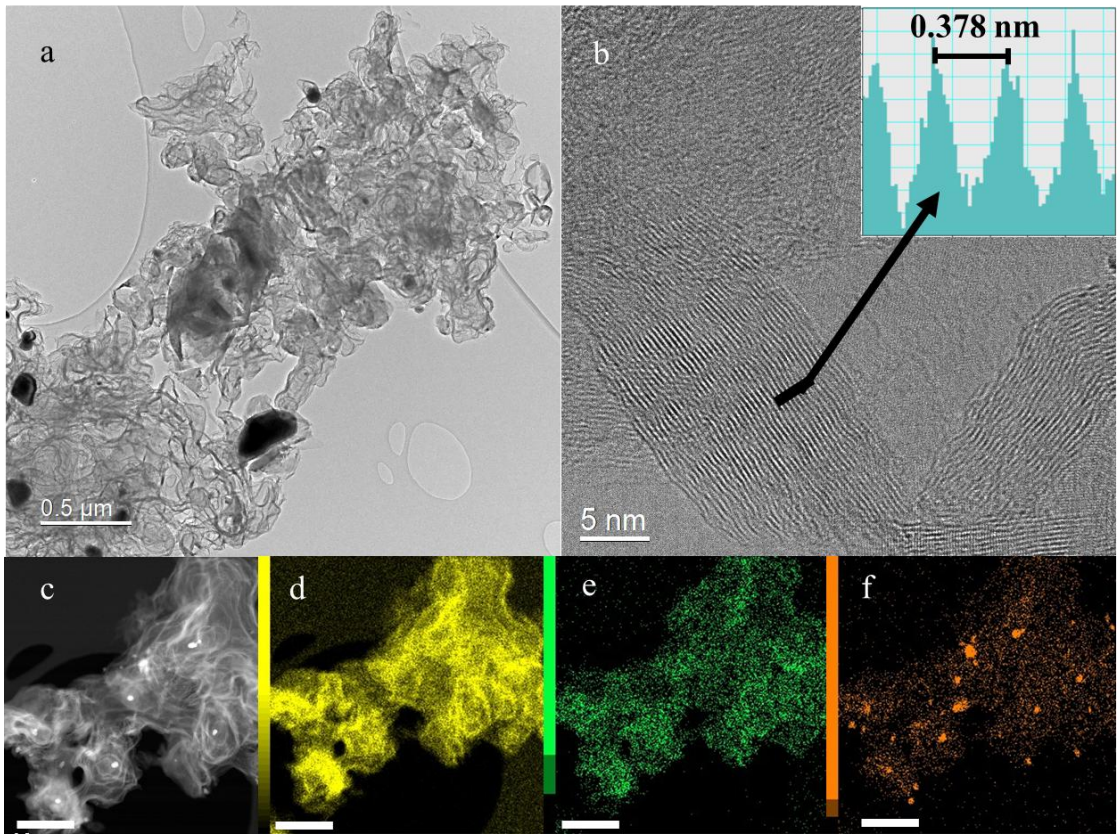

Figure S6: (a,b) HRTEM images of NC@Fe_3C-800 at two different magnifications. As in the case of NC@Fe_3C, there are graphitic regions devoid of Fe_3C nanoparticles due to the HCl washing step. (c) STEM (HAADF) images of NC@Fe_3C material and EDX mapping of elements (d) C, (e) N and (f) Fe, with scale bars of 200 nm.

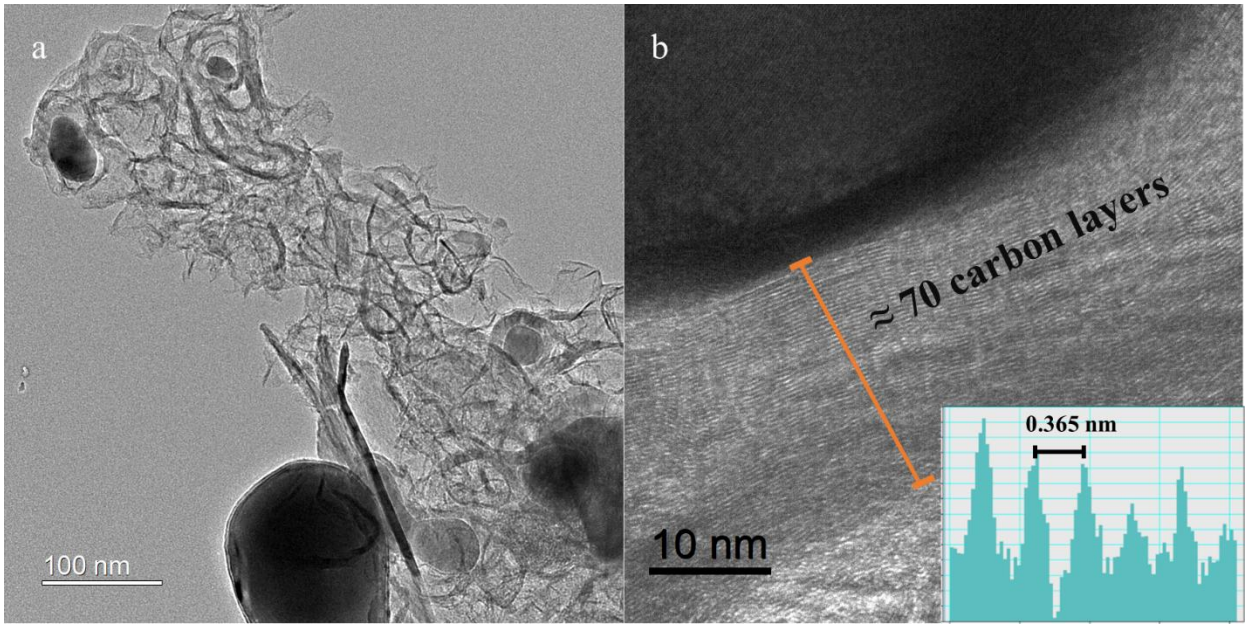

Figure S7: HRTEM image of NC@Fe_3C-1000 at two different magnifications.

Table S3: Textural properties of carbonaceous materials obtained from the treatment of N_2 and H_2 adsorption isotherm data.

Sample	$S_{2D\text{-}NLDFT}$ ($m^2\ g^{-1}$)	V_T ($cm^3\ g^{-1}$)	V_{MESO} ($cm^3\ g^{-1}$)	V_{MIC} ($cm^3\ g^{-1}$)
C_1N_1	280	0.30	0.22	0.08
NC@Fe_3C-500	40	0.14	0.14	0.00
NC@Fe_3C-700	130	0.24	0.21	0.03
NC@Fe_3C-800	310	0.54	0.46	0.08
NC@Fe_3C-900	320	0.54	0.45	0.09
NC@Fe_3C-1000	330	0.57	0.49	0.08

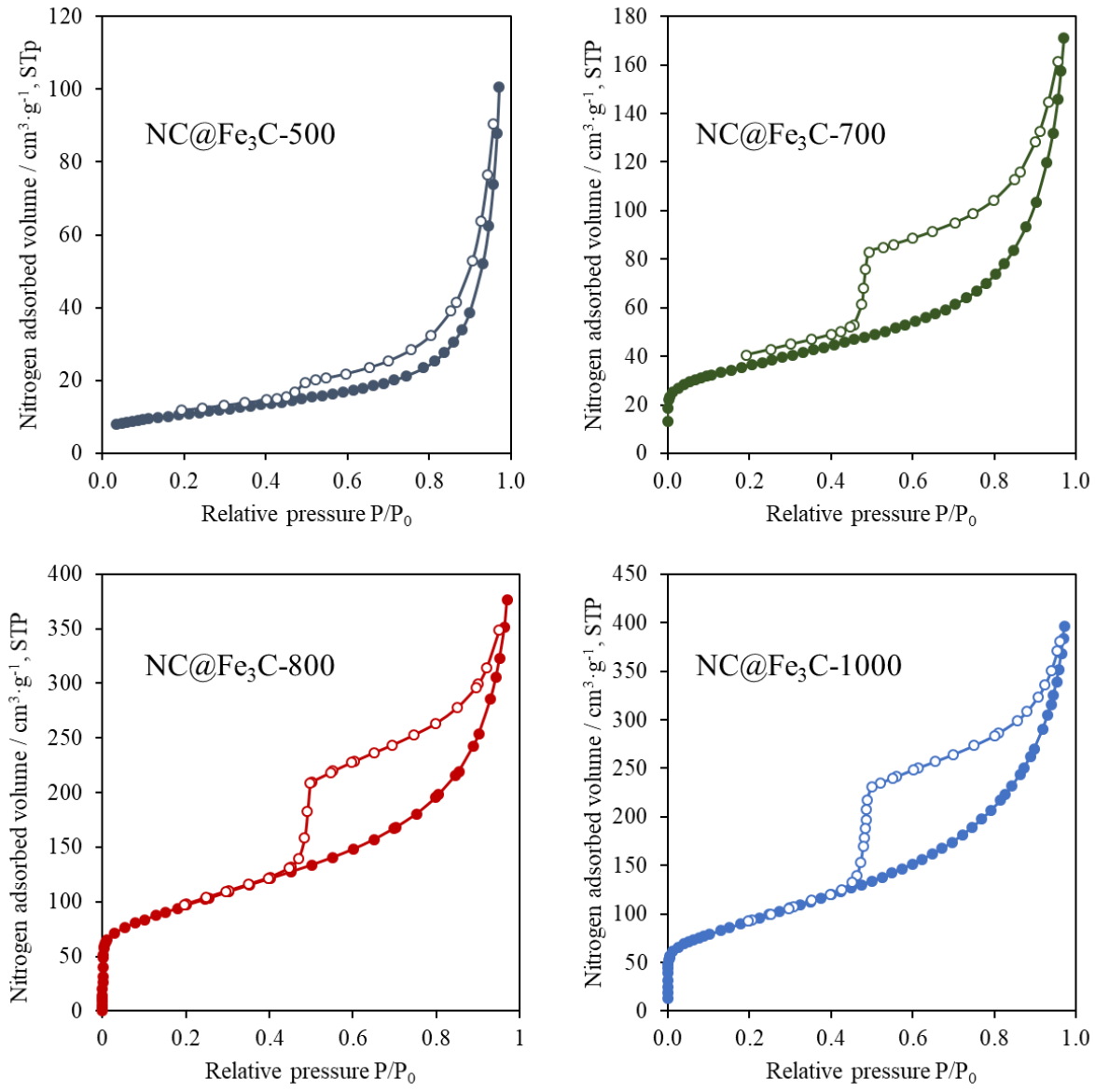

Figure S8: N_2 adsorption-desorption isotherms at -196 ºC for NC@Fe_3C-*T* materials.

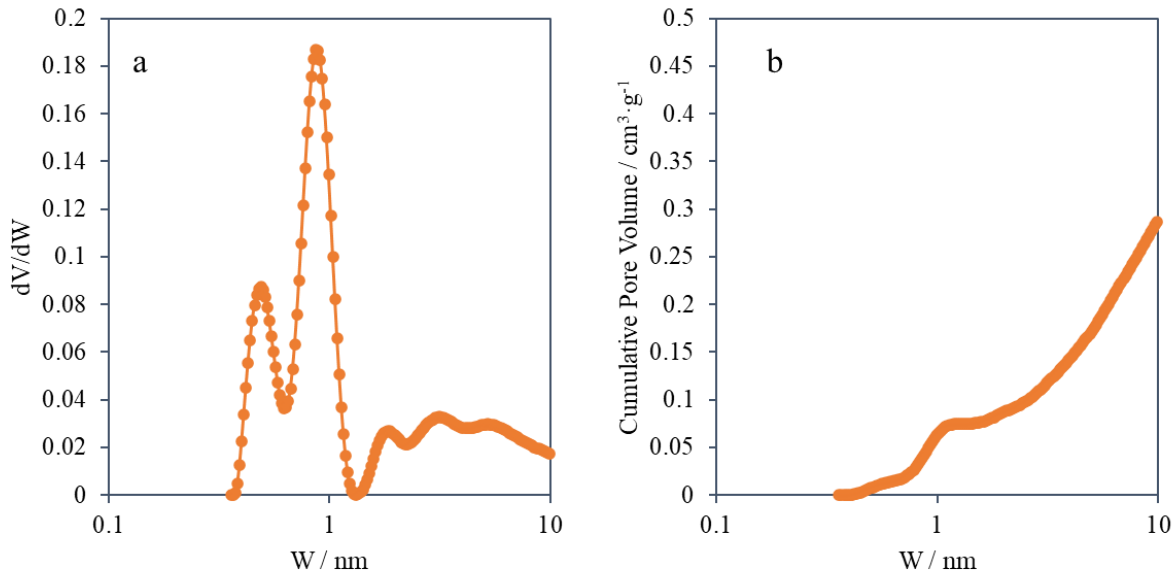

Figure S9: (a) Pore size distribution and (b) cumulative pore volume of NC@Fe_3C-900, obtained from N_2 adsorption-desorption isotherms at -196 ºC.

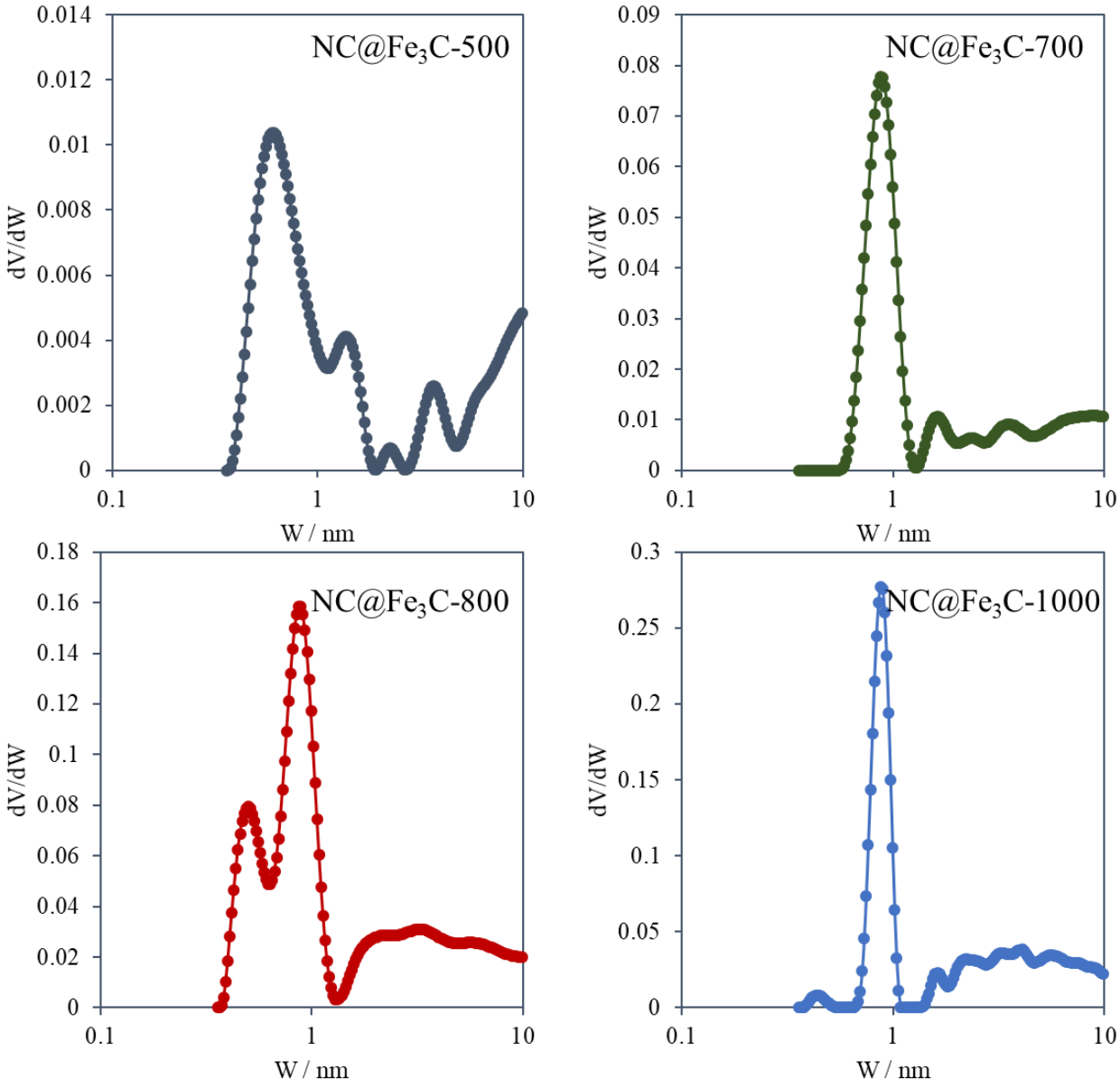

Figure S10: Pore size distributions of NC@Fe_3C-*T* materials obtained from N_2 adsorption-desorption isotherms at -196 ºC.

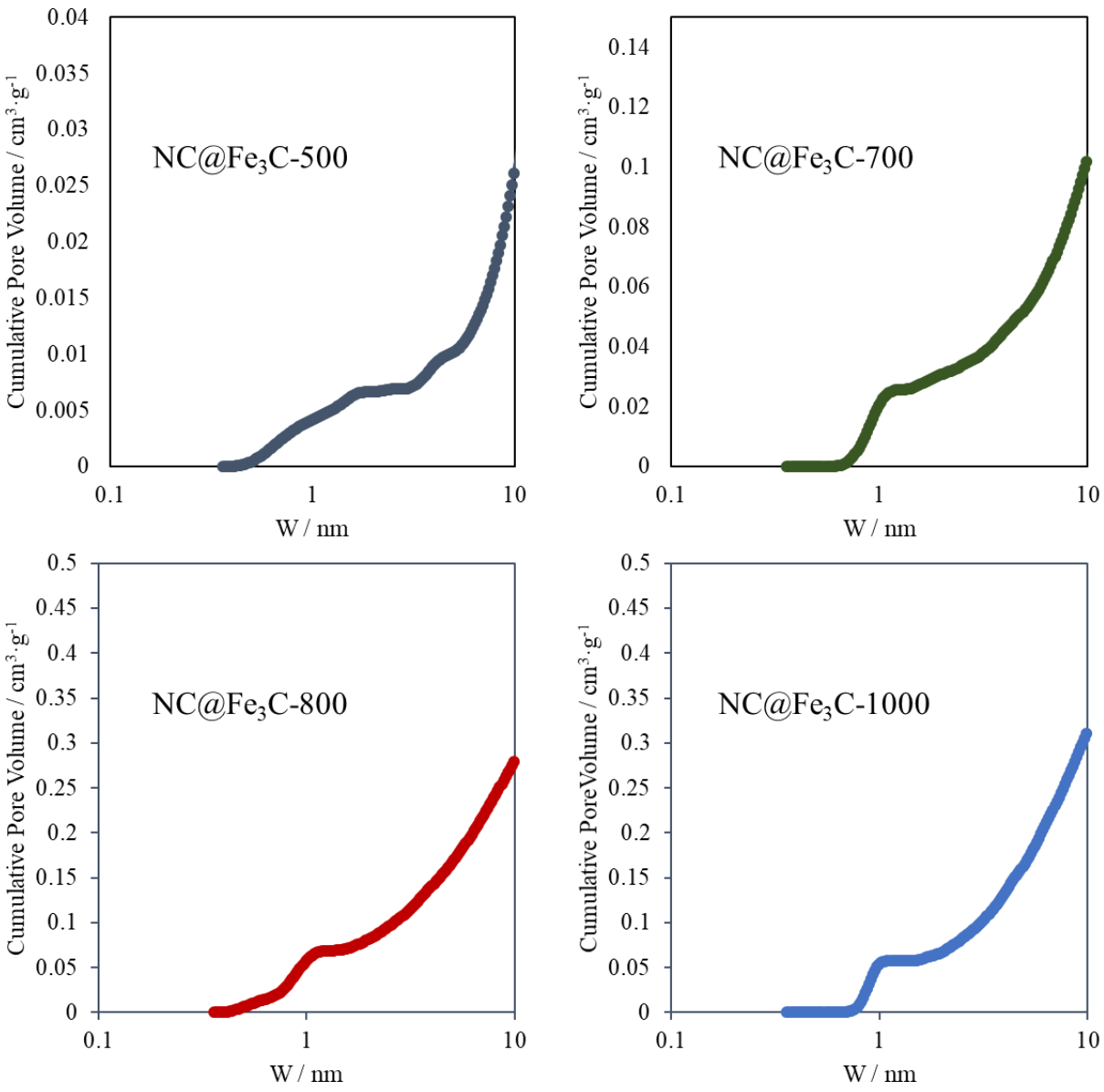

Figure S11: Cumulative pore volumes of NC@Fe_3C-*T* materials obtained from N_2 adsorption isotherms at -196 ºC.

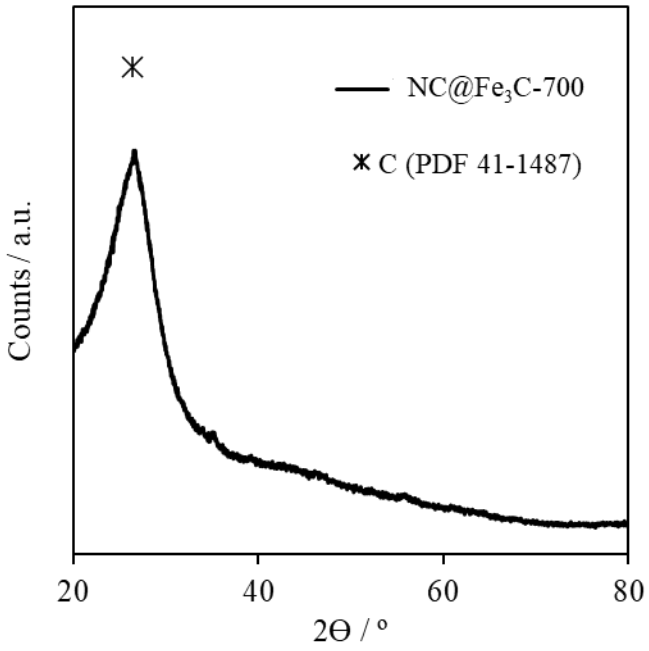

Figure S12: XRD pattern of NC@Fe_3C-700.

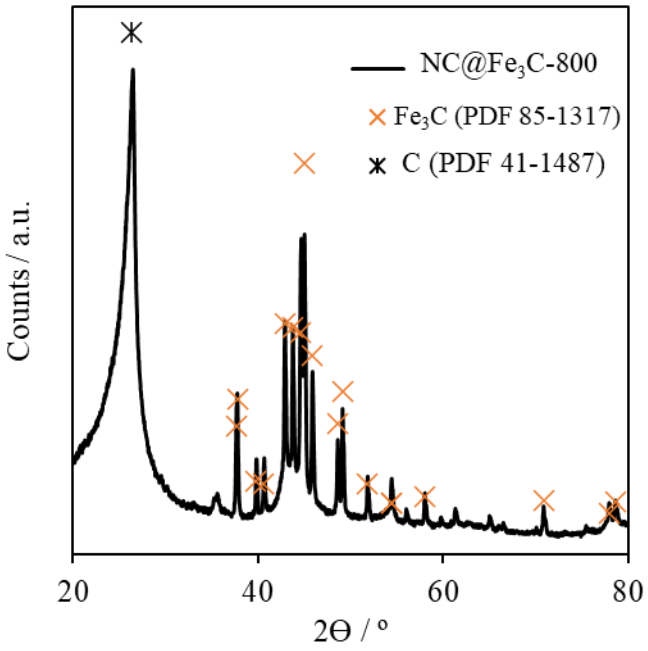

Figure S13: XRD pattern of NC@Fe_3C-800.

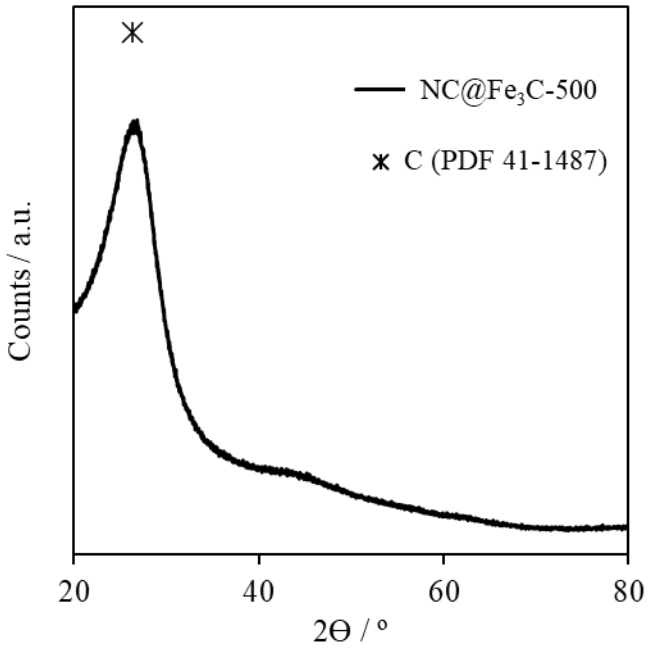

Figure S14: XRD pattern of NC@Fe_3C-500.

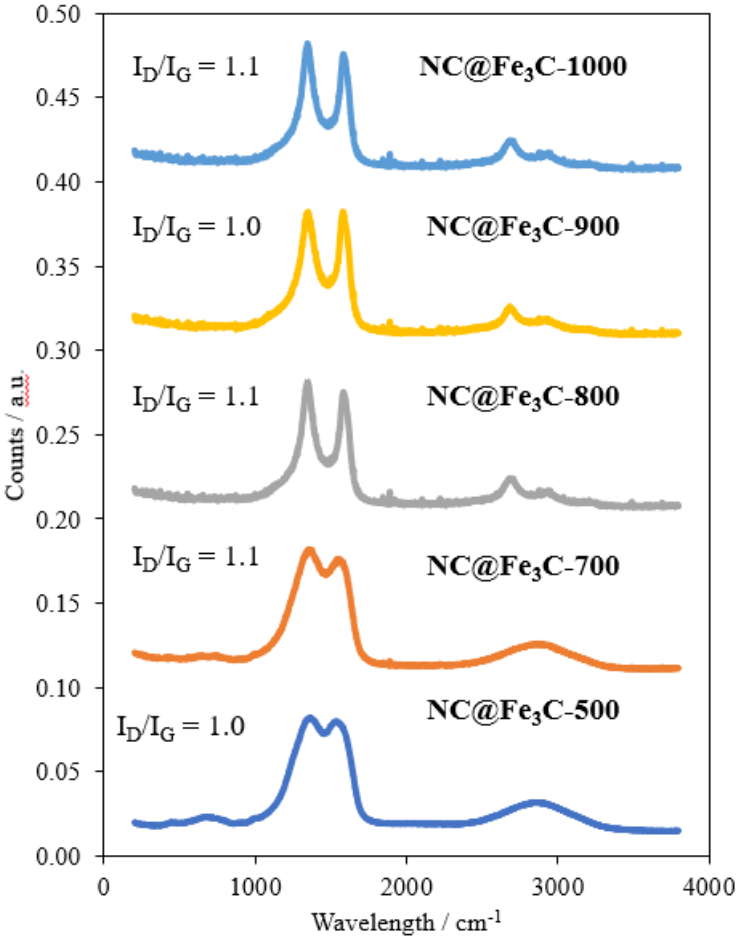

Figure S15: Raman spectra at 532 nm of all NC@Fe_3C-*T* materials.

Table S4: Carbon, nitrogen, oxygen and iron contents, determined by XPS. Graphitic N is obtained from the deconvolution of the N 1s spectra.

Sample	*C content / at.%*	*N content / at.%*	*O content / at.%*	*Fe content / at.%*	*Graphitic N / %*
NC@Fe_3C-500	61.1	31.8	6.7	0.4	-
NC@Fe_3C-700	71.6	20.7	7.0	0.7	5
NC@Fe_3C-800	91.8	3.5	4.6	0.1	30
NC@Fe_3C-900	94.5	2.4	3.0	0.1	38
NC@Fe_3C-1000	93.7	2.9	2.1	0.2	41

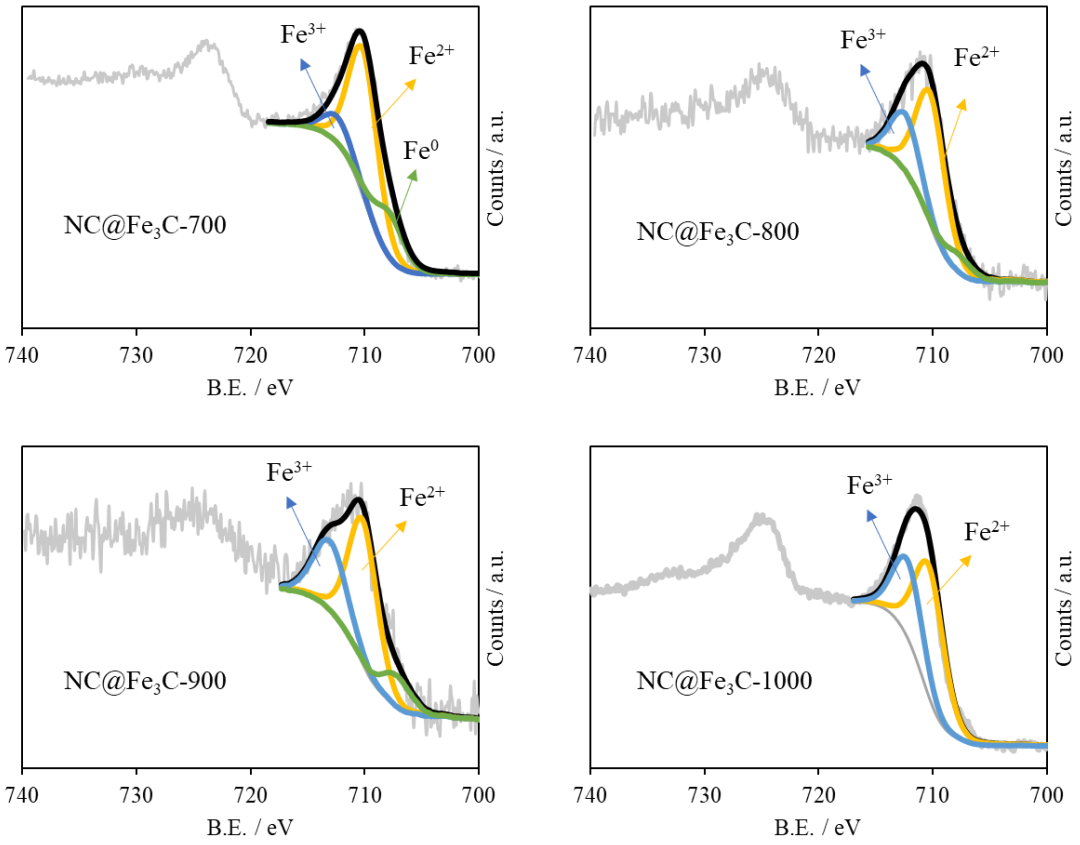

Figure S16: Fe 2p 3/2 XPS spectra of all NC@Fe_3C-*T* materials. The green peak represents metallic Fe^0, the yellow peak represents Fe^{2+}, and the blue peak represents the oxidation state Fe^{3+}.

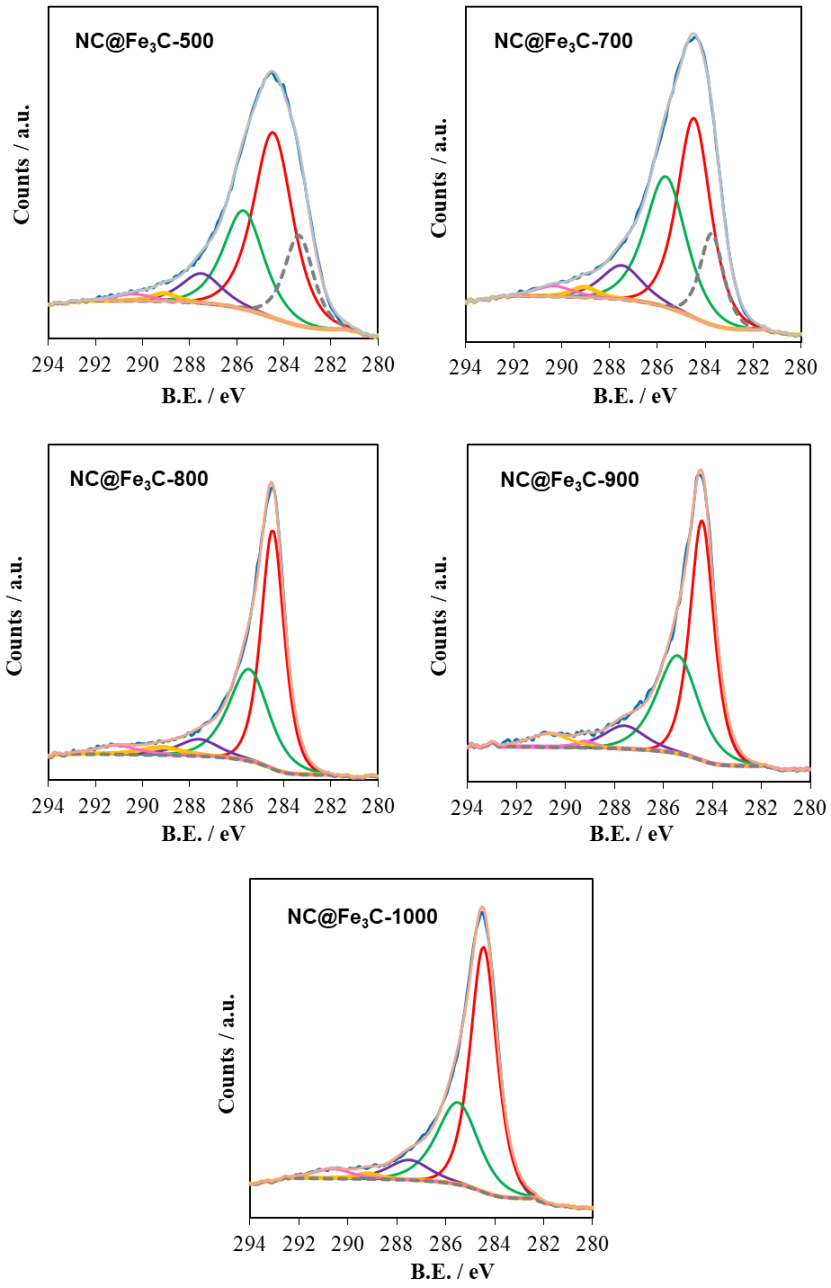

Figure S17: C 1s XPS spectra of all NC@Fe_3C-*T* materials. The red peaks represent C=C species, the green peaks represent C-O species, and the violet peaks represent C=O species. Note: The higher the heat treatment temperature, the greater the C=C contribution, indicating an increase in C content and a higher graphitization degree.

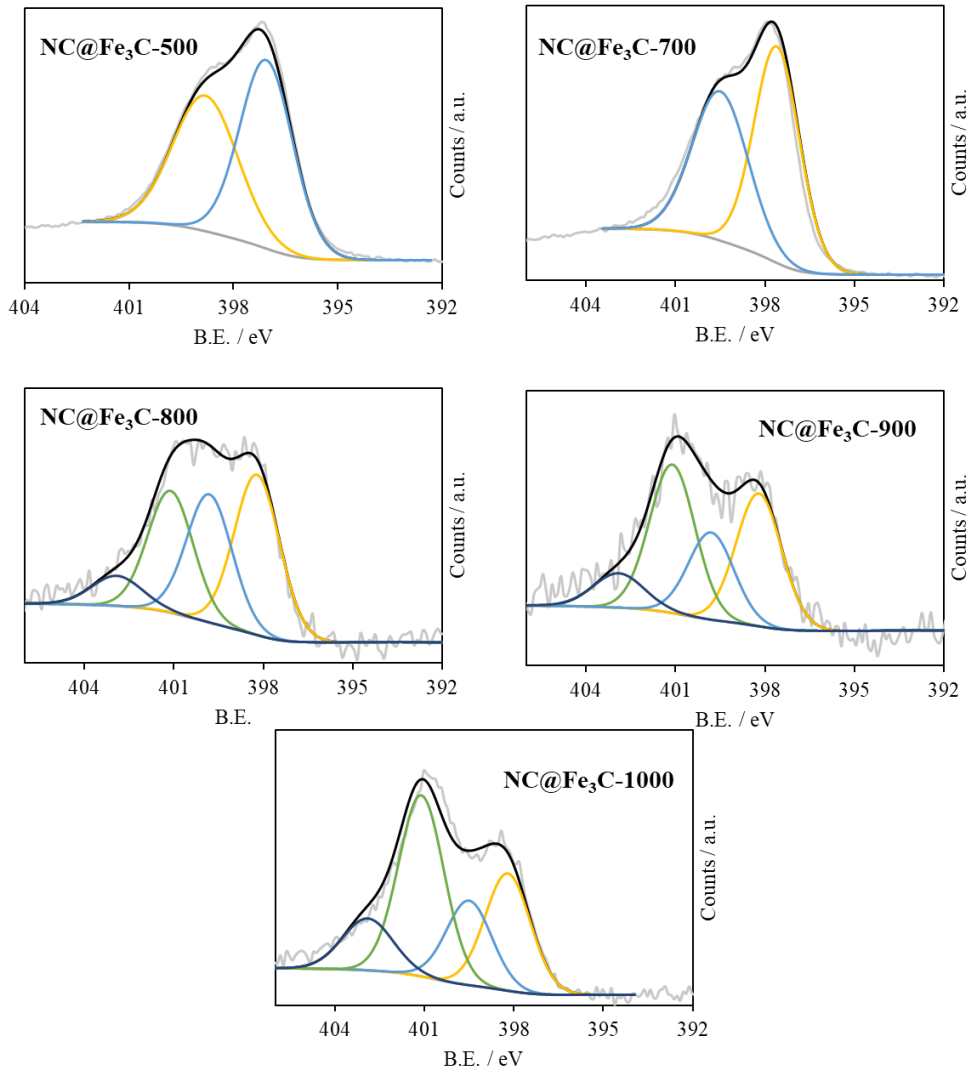

Figure S18: N 1s XPS spectra of all NC@Fe_3C-*T* materials. The yellow peaks represent pyridinic N species, the blue peaks represent Fe-N-type species, the green peaks represent graphitic N species, and the violet peaks represent N-O species. Note: As observed, increasing the temperature during heat treatment leads to a greater contribution of graphitic N species.

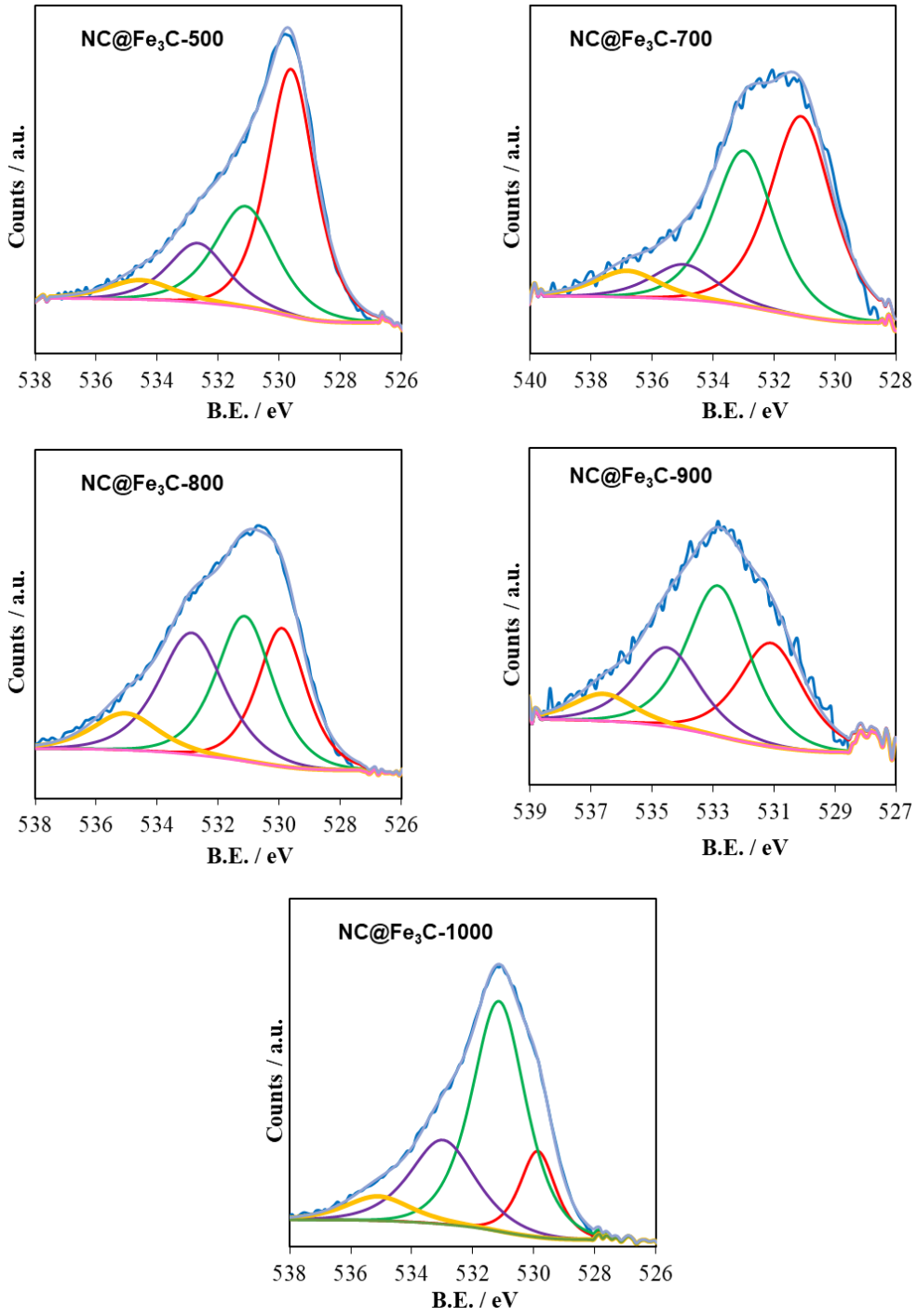

Figure S19: O 1s XPS spectra of all NC@Fe_3C-*T* materials. The red peaks represent O(I) species, the green peaks represent O(II) species, the violet peaks represent O(III) species, and the yellow peaks represent O(IV) species. Note: Increasing temperature during the heat treatment leads to a decrease in O(I) species, as well as an increase in O(III) content.

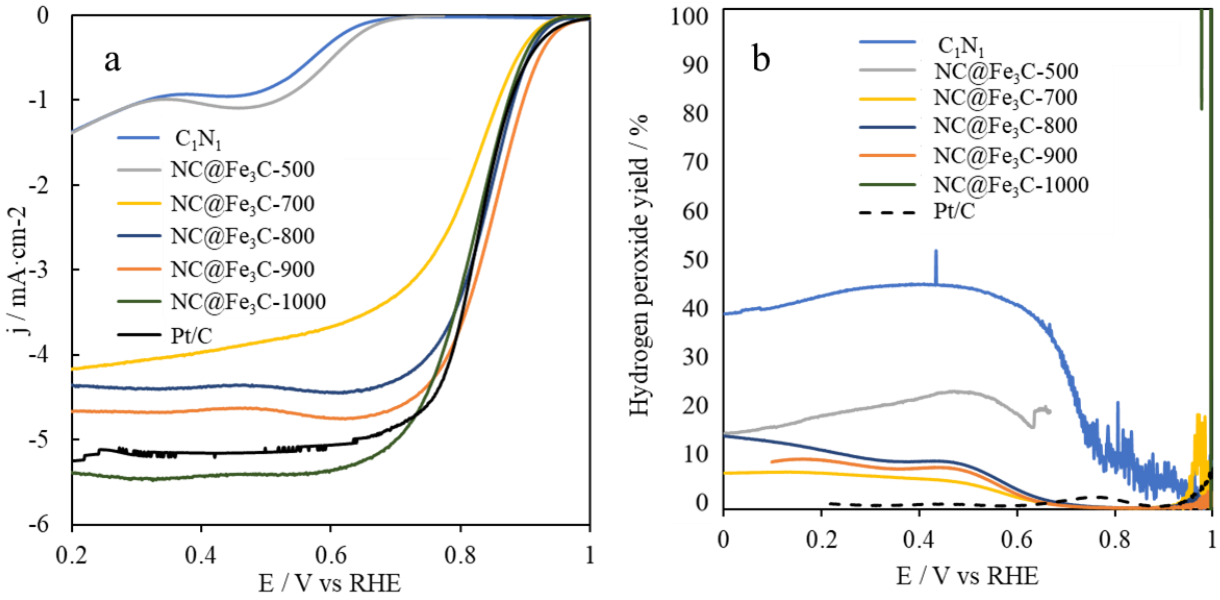

Figure S20: (a) LSV curves, and (b) hydrogen peroxide yield of all NC@Fe_3C-*T* materials obtained at 5 mV·s^{-1} and 1600 rpm in an O_2-saturated 0.1 M KOH solution.

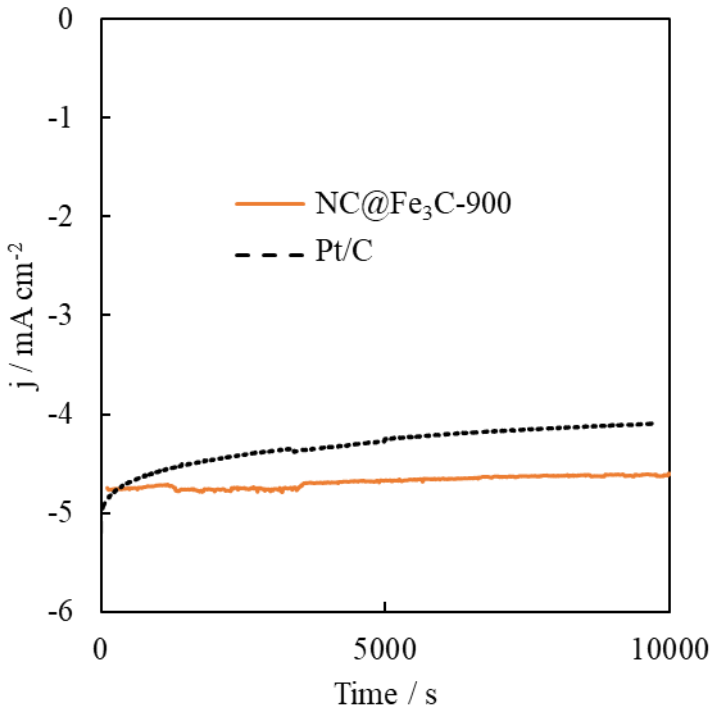

Figure S21: Chronoamperometric response of NC@Fe_3C-900 and Pt/C in an O_2-saturated 0.1 M KOH solution at 1600 rpm.

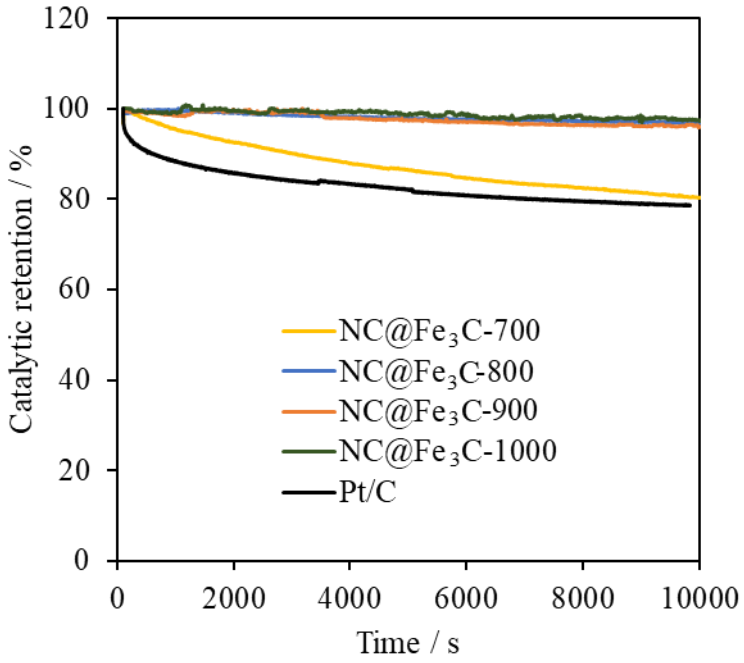

Figure S22: Chronoamperometric response of all NC@Fe_3C-*T* materials at a fixed potential of 0.5 V vs RHE in an O_2-saturated 0.1 M KOH solution and at 1600 rpm.

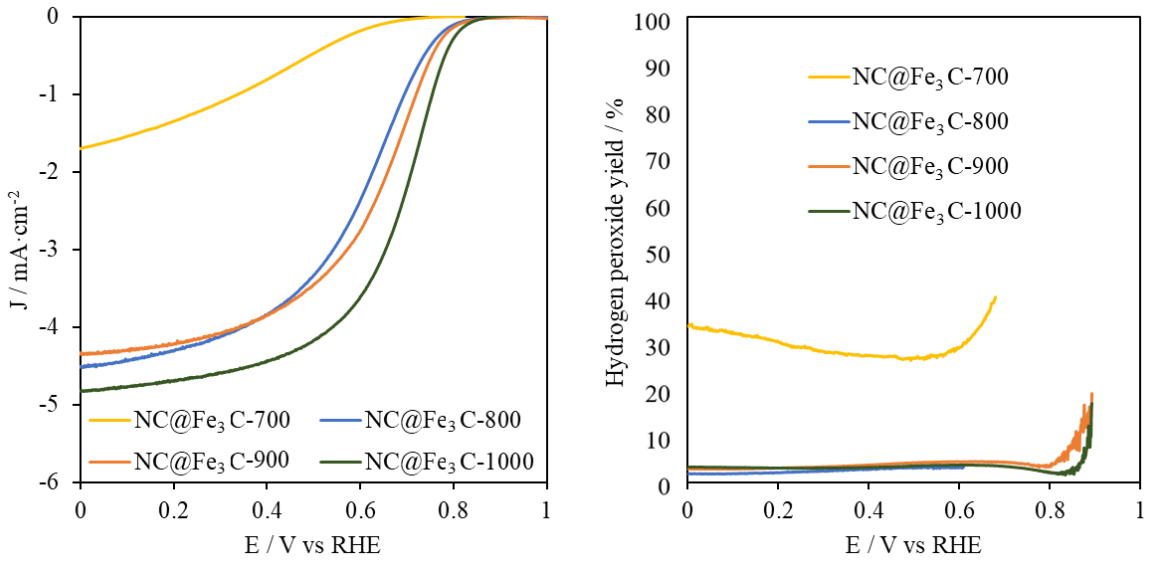

Figure S23: (a) LSV curves, and (b) hydrogen peroxide yield of all NC@Fe_3C-*T* materials obtained at 5 mV·s^{-1} and 1600 rpm in an O_2-saturated 0.5 M H_2SO_4 solution.

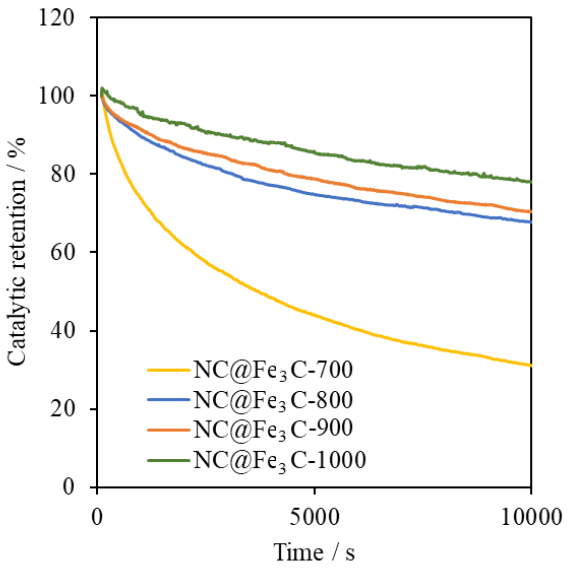

Figure S24: Chronoamperometric response of all NC@Fe_3C-*T* materials at a fixed potential of 0.5 V vs RHE in an O_2-saturated 0.5 M H_2SO_4 solution and at 1600 rpm.

Table S5. Free energy variation at U = 1.23 V of reaction intermediates (*OOH, *O, *OH, and *). Values in red determines the rate-determining step (RDS).

Model system	*OOH / eV	*O / eV	*OH / eV	* / eV
C	2.17	-1.05	0.17	-1.29
C@Fe_3C	0.98	-1.71	1.03	0.30
NC	0.89	-0.91	-0.05	0.07
NC@Fe_3C	0.72	-1.70	0.70	0.28
2NC@Fe_3C	0.84	-1.09	0.13	0.12

Table S6. Gibbs free energies of ORR intermediates (*OOH, *O, and *OH) represented by equations (S2) to (S4), and the ORR theoretical overpotential (η_{ORR}) calculated for each selected system. The ORR theoretical overpotential is calculated as the energy required to overcome the rate-determining stage.

Model system	*OOH / eV	*O / eV	*OH / eV	η_{ORR} / eV
C	5.86	3.58	2.52	2.17
C@Fe_3C	4.67	1.73	1.53	1.03
NC	4.58	2.44	1.16	0.89
NC@Fe_3C	4.41	1.48	0.95	0.72
2NC@Fe_3C	4.53	2.21	1.11	0.84

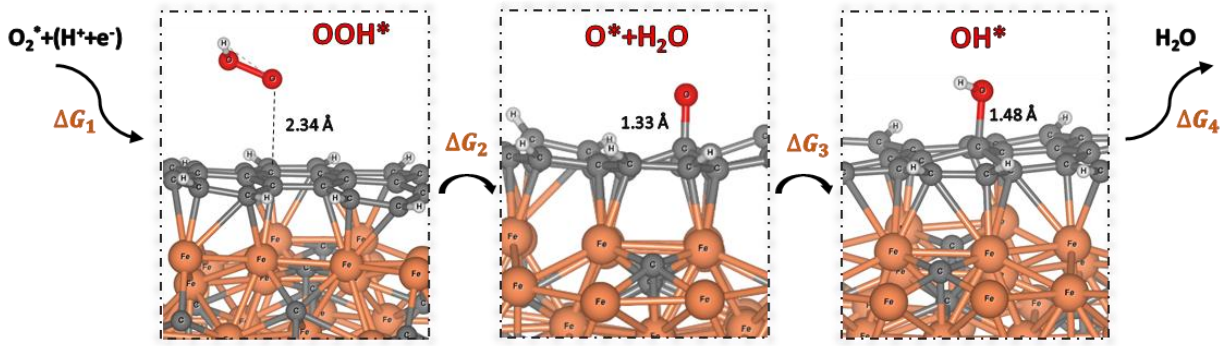

Figure S25: Illustration of all ORR intermediates for the C@Fe_3C model system.

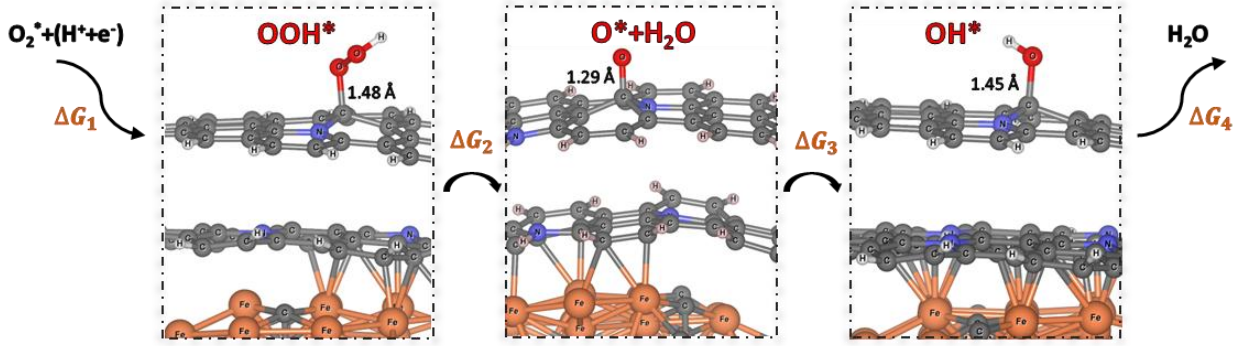

Figure S26: Illustration of all ORR intermediates for the 2NC@Fe_3C model system.

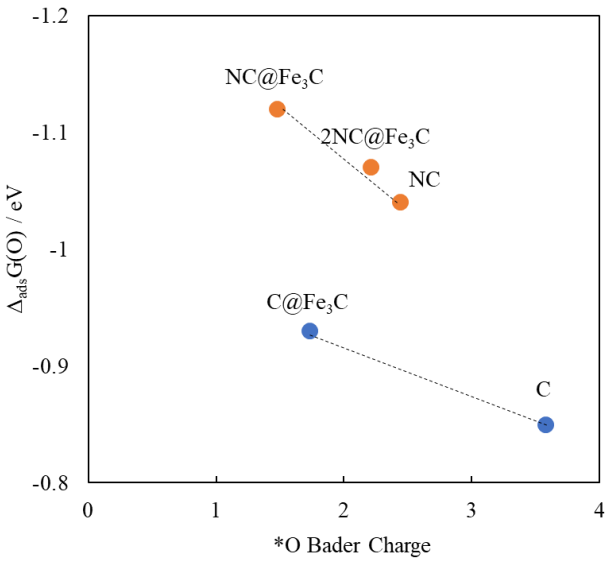

Figure S27: Schematic representation of the correlation between the Bader charge calculated on the *O intermediate and the Gibbs free energy calculated for oxygen adsorption ($\Delta_{ads}G$ (O)) for both undoped C and C@Fe_3C (represented by orange circles) and NC, NC@Fe_3C and 2NC@Fe_3C (represented by blue circles) model systems.

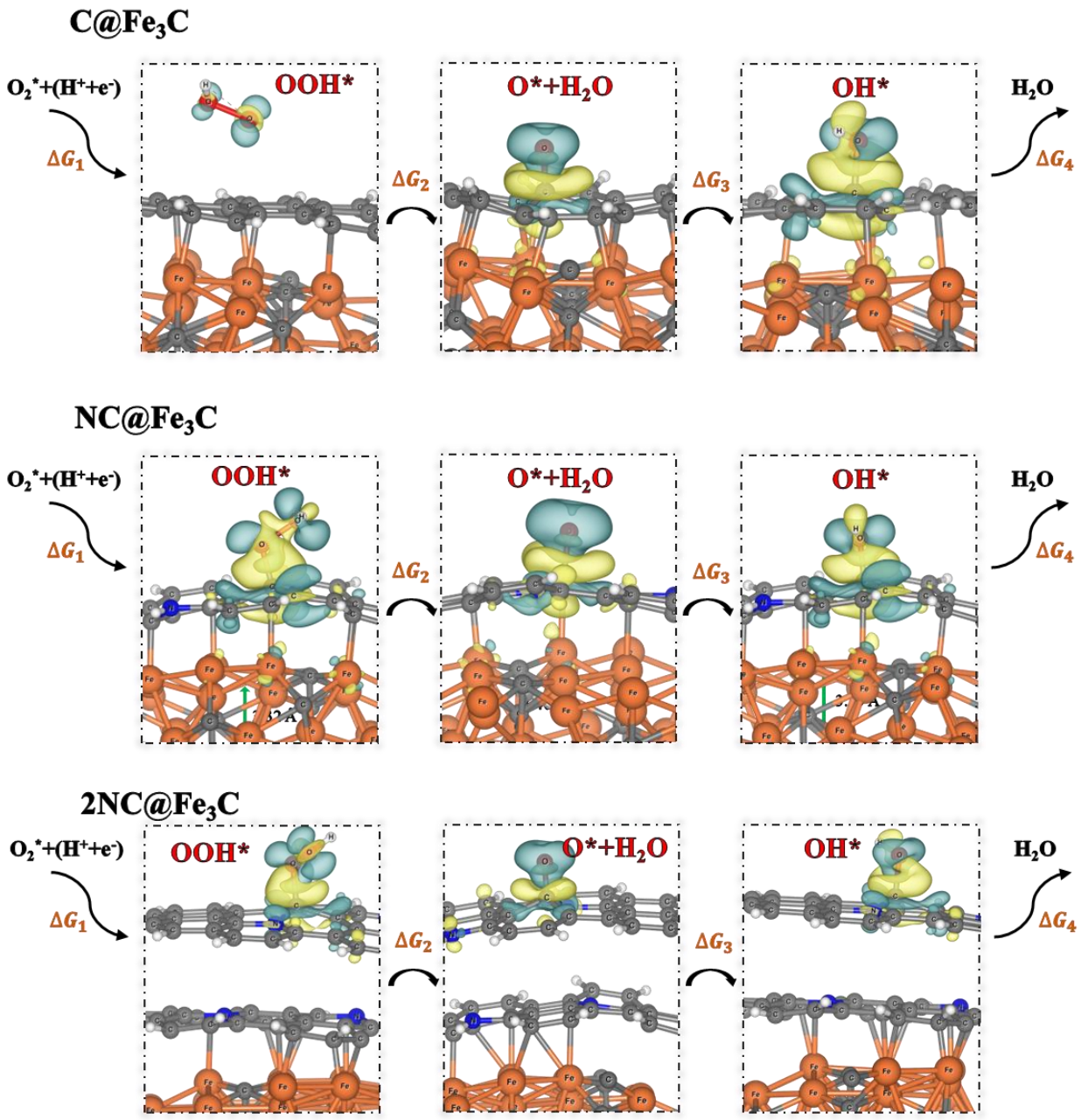

Figure S28: Isosurfaces of electron density change (Δρ). Blue areas indicate an increase in electron density, while yellow areas indicate a decrease in electron density.

Table S7: Bader charges of Fe_3C core, N-doped carbon layer, and O atoms for C@Fe_3C, NC@Fe_3C and 2NC@Fe_3C at each step of the reaction.

C@Fe_3C	**OOH***	**O***	**OH***
Fe_3C core	0.02	0.08	0.03
N-doped carbon layer	0.03	0.80	0.36
O atom	-0.14	-0.93	-0.48
O atom	-0.05		

NC@Fe_3C	**OOH***	**O***	**OH***
Fe_3C core	0.06	0.26	0.18
N-doped carbon layer	0.43	0.78	0.41
O atom	-0.44	-1.12	-0.68
O atom	-0.12		

2NC@Fe_3C	**OOH***	**O***	**OH***
Fe_3C core	0.03	0.16	0.11
N-doped carbon layer	0.40	0.79	0.43
O atom	-0.33	-1.06	-0.56
O atom	-0.15		

[1] B. Ravel, M. Newville, *J. Synchrotron Radiat.* **2005**, *12*, 537.

[2] P. Ramirez-Vidal, R. L. S. Canevesi, G. Sdanghi, S. Schaefer, G. Maranzana, A. Celzard, V. Fierro, *ACS Appl Mater Interfaces* **2021**, *13*, 12562.

[3] L. Bouleau, S. Pérez-Rodríguez, J. Quílez-Bermejo, M. T. Izquierdo, F. Xu, V. Fierro, A. Celzard, *Carbon N Y* **2022**, *189*, 349.

[4] A. L. Gonçalvez Biancolli, D. Herranz, L. Wang, G. Stehlikova, R. Bance-Soualhi, J. Ponce-Gonzalez, P. Ocon, E.A. Ticianelli, D.K. Whelligan, J.R. Varcoe, E.I. Santiago, *J Mater Chem A Mater* **2018**, *6*, 24330.

[5] X. Peng, Y. H. D. Kulkami, T. J. Omasta, B. Ng, Y. Zheng, L. Wang, J. M. LaManna, D. S. Hussey, J. R. Varcoe, I. V. Zenyuk, W. E. Mustain, *Nat Commun* **2020**, *11*, 3561.

[6] M. Mandal, G. Huang, P. A. Kohl, *J Memb Sci* **2019**, *570–571*, 394.

[7] G. Huang, M. Mandal, N. U. Hassan, K. Groenhout, A. Dobbs, W. E. Mustain, P. A. Kohl, *J Electrochem Soc* **2020**, *167*, 164514.

[8] G. Huang, M. Mandal, N. U. Hassan, K. Groenhout, A. Dobbs, W. E. Mustain, P. A. Kohl, *J Electrochem Soc* **2021**, *168*, 024503.

[9] L. J. Sham, W. Kohn, *Physical Review* **1966**, *145*, 561.

[10] P. Hohenberg, W. Kohn, *Physical Review* **1964**, *136*, B864.

[11] G. Kresse, J. Furthmüller, *Comput Mater Sci* **1996**, *6*, 15.

[12] G. Kresse, J. Hafner, *Phys Rev B* **1993**, *47*, 558.

[13] J. P. Perdew, K. Burke, M. Ernzerhof, *Phys Rev Lett* **1996**, *77*, 3865.

[14] S. Grimme, S. Ehrlich, L. Goerigk, *J Comput Chem* **2011**, *32*, 1456.

[15] S. Grimme, J. Antony, S. Ehrlich, H. Krieg, *J Chem Phys* **2010**, *132*, 154104.

[16] L. Wang, T. Maxisch, G. Ceder, *Phys Rev B* **2006**, *73*, 195107.

[17] G. Henkelman, A. Arnaldsson, H. Jónsson, *Comput Mater Sci* **2006**, *36*, 354.

[18] E. Skúlason, G. S. Karlberg, J. Rossmeisl, T. Bligaard, J. Greeley, H. Jónsson, J. K. Norskov, *Physical Chemistry Chemical Physics* **2007**, *9*, 3241.